I&EC research
Industrial & Engineering Chemistry Research

Article

pubs.acs.org/IECR

Scale Up Production of Nanoparticles: Continuous Supercritical Water Synthesis of Ce−Zn Oxides

Christopher J. Tighe, Raul Quesada Cabrera, Robert I. Gruar, and Jawwad A. Darr*

Christopher-Ingold Laboratories, Department of Chemistry, University College London, 20 Gordon Street, London WC1H 0AJ, United Kingdom

Supporting Information

ABSTRACT: A new continuous supercritical water pilot plant was used for the large-scale production of nanomaterials in the Zn−Ce oxide system. Similar to an existing laboratory continuous process, the pilot plant mixes aqueous solutions of the metal salts at room temperature with a flow of supercritical water (450 °C and 24.1 MPa) in a confined jet mixer, resulting in the formation of nanoparticles in a continuous manner. The Zn−Ce oxide system, as synthesized here under identical concentration conditions than those used in our laboratory scale process (but 17.5 times total flow rate), has been used as a model system to identify differences in particle properties due to the physical enlargement of the mixer. The data collected for the nanoparticles from the pilot plant was compared to previous work using a laboratory scale continuous reactor. In the Ce−Zn binary oxide series, it was shown that Zn had an apparent solubility of about 20 mol% in the CeO_2 (fluorite) lattice, whereafter a composite of the two phases was obtained, consistent with the high solubility observed in previous studies using a continuous hydrothermal process. Because of the inherent scalability of the continuous process and excellent mixing characteristics of the confined jet mixer, it was found that the pilot plant nanoparticles were almost indistinguishable from those made on the laboratory scale.

1. INTRODUCTION

Recent commercial interest in nanomaterials and their applications has led to the development of many new technologies and approaches for synthesis of such materials on increasingly larger scales.[1−3] The production of these materials is often intensive in terms of labor, chemicals, and energy, particularly when scaled up. Many synthesis methods are also lengthy, leading to high running costs associated with factors such as waste processing (for instance, emulsions or toxic organic solvents involved in the production of nanoparticles or quantum dots), safety concerns, cost of reagents, etc.[1−6]

From the point of view of the nanomaterials production, the scale up may significantly alter heat/mass transfer rates, which leads to different regimes for the nucleation and growth of nanoparticles. In this case, the properties of the nanomaterials synthesized (e.g., crystallite size, solid solubility, etc.) could differ from those produced at smaller scales, which may be undesirable for an intended application.[7] In terms of nanoparticle quality (small crystallite size and breadth of size distribution, phase purity, etc.), many efficient processes for making nanomaterials require the sudden conversion of a precursor into a nanomaterial (nucleation-dominated process with little or no particle growth), often leading to metastable phases (with novel properties) that are not readily accessible via more conventional synthesis processes.[3]

From a technical standpoint, the scale up of a process for producing nanomaterials is not trivial as such syntheses often involve very high temperatures and pressures. One promising method for the rapid synthesis of high quality nanoceramics is a continuous hydrothermal flow synthesis (CHFS). In CHFS, a feed of low-density supercritical water (above the critical point of water, T_c = 374 °C and P_c = 22.1 MPa) is mixed with a higher density ambient temperature flow of aqueous metal salts in a confined jet mixer, rapidly converting the metal salts into metal oxide nanoparticles via simultaneous hydrolysis and dehydration reactions.[8] The process does not use any organic solvents, and the products are conveniently recovered as aqueous slurry at ambient temperature (after in-line cooling). This process, or variants of it, has been used for the production of many nanomaterials, e.g., titania and titanate photocatalysts, bioceramics, potential fuel cell cathodes and composite anode nanomaterials, catalysts, and gas sensors, among others.[9−16] The particle properties made using such unique conditions are often difficult to achieve directly using conventional synthesis methods.

Previously, the authors developed a manual high-throughput CHFS system known as HiTCH to increase nanomaterials throughput allowing a complete Ce−Zr−Y phase diagram (66 samples) to be produced and evaluated on a relatively short time scale.[17−21] HiTCH was also used to manufacture a Zn−Ce oxide binary system in which unprecedented solubility of Zn in CeO_2 was observed.[20] In a further development, a fully automated CHFS process allowed the rapid evaluation of nanophosphors.[17] More recently, we reported the synthesis of nanoceramics using a continuous hydrothermal reactor at pilot plant scale (17.5 times scale up on flow rate alone from lab scale).[22,23]

It is well known that the chemical and physical properties of nanoceramics can be tuned by doping a metal oxide structure with various elements.[24−27] Doping can introduce significant

Received: September 20, 2012
Revised: January 22, 2013
Accepted: February 12, 2013
Published: February 12, 2013

   dx.doi.org/10.1021/ie3025642 | Ind. Eng. Chem. Res. 2013, 52, 5522−5528

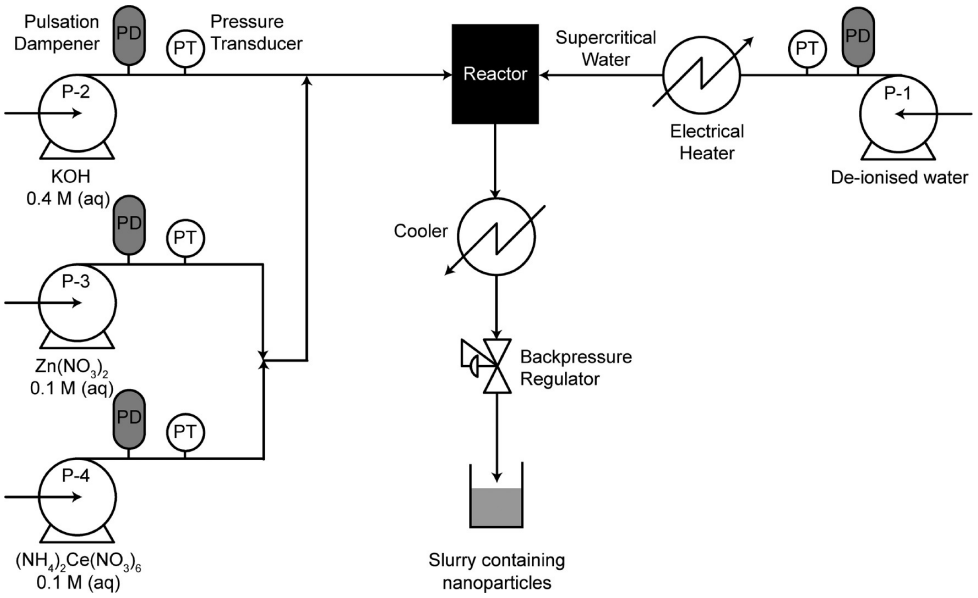

Figure 1. Simplified continuous hydrothermal flow synthesis pilot plant flow diagram.

changes in the structure of the host material, creating various lattice defects such as cation/oxygen vacancies, resulting in different functional properties from those of the host material. The Zn−Ce oxide binary system has attracted interest for applications as UV attenuators and as an up-converting phosphor host material.[28,29] Homometallic CeO_2 (fluorite fm-3m structure) has a bandgap of about 3.0 eV and exhibits several interesting properties such as good optical transparency and strong UV absorption when crystallite dimensions approach the nanoscale. ZnO, a semiconductor with a wide bandgap of about 3.36 eV, is also of interest in a variety of applications as a UV attenuation material as its dimensions approach the nanoscale.[30] Metal-doped Ce oxides (M/CeO_2) find applications as clean catalysts in the oxidation of automotive exhaust, anticorrosion materials, and gas sensors. In these applications, both homogeneous distribution of dopants and high surface areas are vital in their final application.[31] Conventional synthetic routes to Zn−Ce oxides include high-temperature solid-state reactions, high-energy ball milling (high production capacity), precipitation in micro-emulsions, sol−gel syntheses, batch hydrothermal synthesis, etc.[22,32,33] Many of these synthetic processes have been used to assess the effect of dopant substitution and particle size.[33] Nevertheless, the aforementioned methods are often energy or chemically intensive (time consuming, multi-step, etc.) and rarely quoted as scalable processes within the academic literature (with the notable exception of high-energy ball milling).

In the work presented here, the binary Zn−Ce oxide system is used as a model to investigate how particle properties change with volumetric scale-up. Comparisons are drawn between optical properties and phase behavior of this system produced in both laboratory and pilot scale reactors.[20,23]

2. EXPERIMENTAL SECTION

2.1. Materials. Zinc nitrate ($Zn(NO_3)_2{\cdot}6H_2O$, > 98%), cerium ammonium nitrate ($(NH_4)_2Ce(NO_3)_6$, > 98.5%), and potassium hydroxide (KOH, > 85%) were obtained from Sigma-Aldrich (Dorset, U.K.). The synthesis was carried out using deionized water (>15 MΩ resistivity).

2.2. Apparatus and Synthesis. Figure 1 shows a process flow diagram of the new continuous hydrothermal flow synthesis pilot plant, designed to be up to 17.5 times the flow rate of a similar laboratory scale process, as detailed in our previous publications.[8−20,23]

Briefly, the pilot scale CHFS process reported herein consists of four industrial diaphragm-type chemical dosing pumps (Milton Roy, Primeroyal K), identified as P1−P4 in Figure 1. The flow rate from each of the pumps was set at the desired value using a linear actuator, up to a maximum of 0.66 L min^{-1}, by adjusting the volume of fluid displaced on each stroke. The error in the flow rate quoted by the manufacturer was ±1% of the maximum, i.e., ± 6.6 mL min^{-1}. In this study, 350 mL min^{-1} of deionized water was pumped (pump P-1) through a custom built electrical heater arrangement (Watlow Cast X 2000, maximum thermal output 24 kW) that heated the water in flow to 450 °C at a pressure of 24.1 MPa (i.e., above the critical point of water, T_c = 374 °C and P_c = 22.1 MPa). The supercritical water was subsequently mixed cocurrently with the precursors (issuing from pumps P-2 to P-4 as detailed in Table S2 of the Supporting Information) in a confined jet reactor.[23] Briefly, the supercritical water entered the inner pipe (1/4 in. OD, 0.049 in. wall thickness) at the bottom of the reactor. The precursors were fed in below the outlet of the supercritical water, which exited the inner pipe as a turbulent jet, and rapid entrainment of the precursor into the supercritical water feed occurs as discussed in our other publication.[23] The mixture at a temperature of 337 °C subsequently flowed upward through tubing (3/4 in. OD, 0.103 in. wall thickness, length 0.5 m), before entering two cooled pipe sections in series (1/4 in. OD, 0049 in. wall thickness, length 1.5 m each). Type K thermocouples were located before and after these cooling pipes and were used to monitor the reactor and product stream temperatures. The cooling system was composed of an outer jacket through which water (supplied by a recirculating chiller) flowed at 100 L min^{-1} and an inlet temperature of 15 °C. At these conditions, the cooling water exited the heat exchanger at approximately 20 °C. The design of the cooler was identical to that which has been previously described in detail on the lab scale apparatus, except the total length was 3 m and the outer

dx.doi.org/10.1021/ie3025642 | Ind. Eng. Chem. Res. 2013, 52, 5522−5528

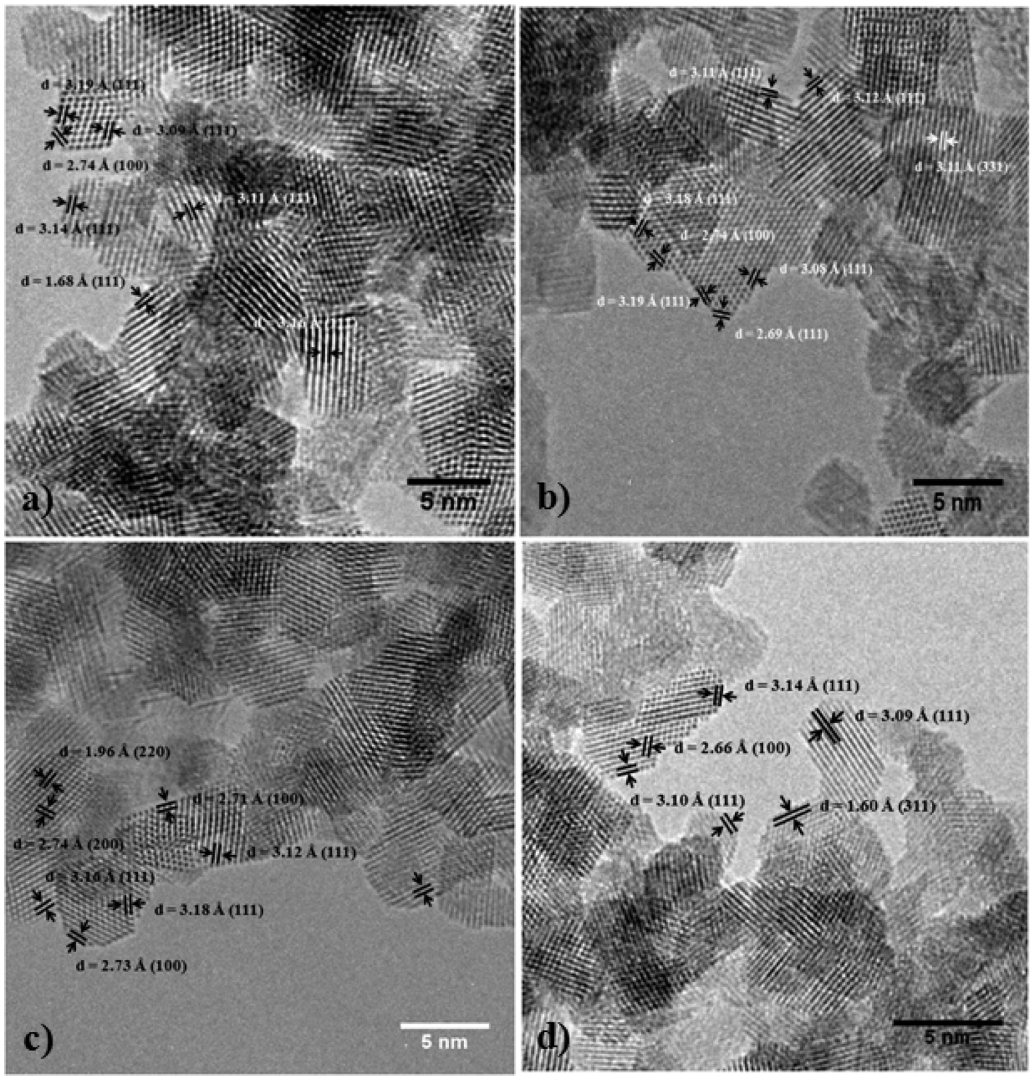

Figure 2. High resolution transmission electron micrograph images of (a) pure CeO_2 and Zn-doped ceria samples with (b) 10 mol% Zn, (c) 20 mol % Zn, and (d) 30 mol% Zn. All samples were produced using a continuous hydrothermal flow synthesis pilot plant process. Interatomic spacing and corresponding Miller indices are noted on each figure (scale bar 5 nm, magnification x 350000).

diameter of the cooling water jacket was 25.4 mm.[8−20] Further details of the design and safety considerations associated with this pilot plant can be found in our other publication.[23]

The zinc and cerium salts, both at the same concentration of 0.1 M used in the author's previous work, were mixed in the different ratios to yield a total flow of 175 mL min^{-1}. The outputs of each of the metal salt precursor pumps are detailed in Table S2 of the Supporting Information.[20] The KOH (0.4 M) flow was pumped at 175 mL min^{-1}. The concentrations of the zinc and cerium salts were matched with those used in the author's previous study.[20] Thus, the mass production rate of nanoparticles collected was 17.5 times that of the laboratory apparatus yielded in the same time.

2.3. Methods. *2.3.1. Sample Post-Treatment.* The nanoparticle laden aqueous slurry was repeatedly centrifuged and washed with deionized water until pH neutral. The concentrated slurry was subsequently dried in a freeze drier (Virtis Genesis 35XL) by slowly heating a sample from −60 to 25 °C over 24 h under a vacuum of 100 mTorr.

2.3.2. Analytical Characterization. X-ray diffraction data were collected using a Bruker D4 Diffractometer (Cu Kα1, λ = 1.540598 Å). Yttria (Y_2O_3) was used as standard for the estimation of instrumental peak broadening. Refinement of the XRD data was performed using GSAS. Elemental analysis was performed using Oxford Instruments Inca 300 energy dispersive X-ray (EDX) detector connected to a JEOL JSM-6300 scanning electron microscope. Samples were prepared for TEM by dispersing the particles ultrasonically in ethanol (99.9%, Sigma-Aldrich, Dorset U.K.) and dropping onto Holey carbon film grids 400 mesh (Agar Scientific, U.K.). A JEOL 4000x transmission electron microscope (350 KeV accelerating voltage) was used for generating HRTEM micrographs of particles and images were captured using a coupled CCD camera (GATAN). Similarly, SAED patterns were taken using a GATAN CCD camera. Image analysis was performed using freely available software ImageJ. Brunauer−Emmett−Teller (BET) surface area measurements were carried out using N_2 in a Micrometrics ASAP 2420 instrument with six analysis stations. The samples were degassed at 120 °C (12 h) under vacuum before the BET measurements. Raman spectra were collected in a Renishaw InVia Raman spectrometer equipped with a 785 nm diode laser. The laser power was 80 mW for all samples, except for pure ZnO and pure CeO_2, which was at 40 mW. The Raman system was calibrated against the silicon

dx.doi.org/10.1021/ie3025642 | Ind. Eng. Chem. Res. 2013, 52, 5522−5528

mode centered at 520 cm^{-1} (spectral resolution 1 cm^{-1}). Absorption spectra were collected using an Ocean Optics USB4000 UV−visible spectrophotometer with a deuterium−halogen (DH2000-BAL) light source. Spectralon was used as a reference material. Color data was obtained from reflectance spectra using the Ocean Optics Spectrasuite software and a D65 light source.

3. RESULTS AND DISCUSSION

Typical reaction yields in the synthesis of the Zn−Ce oxide system were >99% for the series up to 50 mol% Zn, although the yield decreased to 60−80% for samples with higher Zn content. A gradual color change upon Zn content was observed in the freeze-dried powders from yellow CeO_2 to white ZnO. Colorimetric data of all Zn−Ce oxide samples are shown in Figure S1 of the Supporting Information.

The particle size distribution and morphology of selected samples was assessed by TEM (pure CeO_2 and 10, 20, and 30 mol% Zn samples are presented in Figure S2, Supporting Information). The particle size distributions (S.D.) determined for the series were 4.8 (±1.2), 3.2 (±1.1), 3.3 (±2.3), and 3.7 (±1.0) nm, respectively, showing very similar morphology. The presence of a single phase up to a Zn concentration of 30 mol% was confirmed by SAED (Figure S3, Supporting Information). Table S1 of the Supporting Information provides the corresponding summary of the measured lattice spacings and indexed reflections. A slight increase in the lattice parameters of CeO_2 were observed up to 30 mol% Zn, which is consistent with incorporation of Zn into the fluorite lattice. Minor reflections from ZnO (wurtzite structure) were identified at 30 mol% Zn content (Figure S2, Supporting Information). The single crystalline structural details of the $Ce_xZn_{1-x}O_{2-\delta}$ nanomaterials produced using the pilot scale CHFS process were further characterized by HRTEM. Highly crystalline and faceted materials were visualized with no evidence of any significant amorphous content within the particles (Figure 2). The facets observed were typical of those for these materials and were consistent with our previous study.[20] Surface facets were predominantly [111] and [100] (visualization along the [110] zone axis) as highlighted in Figure 2 and are consistent with the crystal habit of CeO_2 showing a fluorite structure. Lattice fringe spacings were consistent with those reported for the CeO_2 fluorite structure. Surveys of the images did not show lattice spacings characteristic of ZnO (expected *d*-spacings of the (100) and (002) planes to be larger).

As discussed further in our previous report, the solubility of Zn in the fluorite may be due to the rapid precipitation of products, allowing nanosized metastable phases to be obtained.[3,20] However, the solubility of Zn in the CeO_2 lattice is certainly limited by the ionic radii mismatch of Ce^{4+} and Zn^{2+} ions, estimated as −23.7% ($(r_{dopant} - r_{host})/r_{host}$), that has restricted Zn content below 10 mol% so far, although values as high as 20 mol% have been claimed in the literature.[20,31,33]

An evaluation of nominal and measured Zn content in the samples (Figure 3) was performed after the determination of Zn:Ce ratios from EDX analysis (Table 2, Supporting Information). The largest divergence was found in the nominally 10 mol% Zn sample (measured 5.08 mol% Zn), which could be due to the slightly lower conversion of the Zn precursor with respect to Ce. The most accurate value was found for the 30 mol% case (29.75 mol% Zn), and a Zn content average difference of 0.75 mol% was calculated over the whole range.

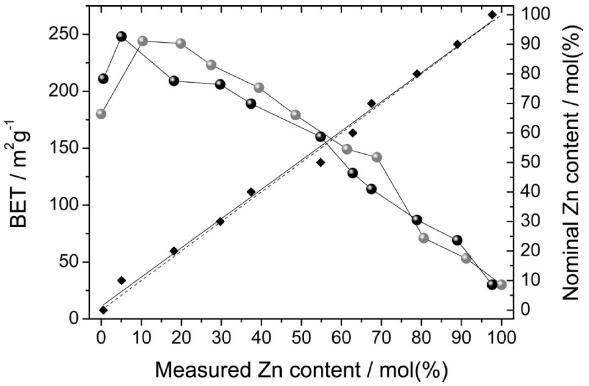

Figure 3. BET surface areas of the Zn−Ce oxide system upon increasing Zn metal content (mol%) as measured from laboratory (gray symbols) and pilot plant (black symbols) scale processes.[20] A linear fit between nominal and measured Zn content from EDX analysis (dashed line) is compared to the target ratio (solid line).

The change in BET surface area of the samples synthesized in the pilot plant was in excellent agreement with the trend observed in our previous report for the laboratory scale process (Figure 3, Table 2, Supporting Information).[20] The BET surface areas measured for pure CeO_2 (211 $m^2\ g^{-1}$) and ZnO (30 $m^2\ g^{-1}$) on the pilot plant significantly exceeded those reported from batch hydrothermal syntheses.[33] The high BET surface area observed for the 10 mol% Zn sample (248 $m^2\ g^{-1}$) was probably due to a decrease in particle size upon substitution of Zn^{2+} for Ce^{4+} cations in the fluorite lattice (0.97 Å versus 0.74 Å).[35] Overall for Zn contents at 30 mol% and more, there is a virtually linear decrease in BET surface area with Zn content (Figure 4). Particle size can be roughly estimated from BET surface area data, assuming the particles are spheres, using $D_S = 6000/(S_{BET}\,\rho)$, where D_S (nm) is the equivalent sphere diameter, S_{BET} ($m^2\ g^{-1}$) is the BET surface area, and ρ (g cm^{-3}) is the density of the material. This calculation resulted in particle diameters of 4 and 41 nm for CeO_2 and ZnO, respectively, which correlate well with the values estimated in the TEM analyses.

The XRD patterns of CeO_2 and Zn-doped CeO_2 with 10 and 20 mol% Zn content ($Zn_{0.1}Ce_{0.9}O_{2-\delta}$ and $Zn_{0.2}Ce_{0.8}O_{2-\delta}$, respectively) were similar. In good agreement with the SAED data for ZnO, sharp X-ray diffraction peaks appeared for the 30 mol% Zn content sample, increasing thereafter with higher Zn concentrations. Le Bail refinements of the XRD data confirmed the structures of CeO_2 (fluorite phase, ICDD pattern 78-694) and ZnO (wurtzite phase, ICDD pattern 79-2205) (Table 3, Supporting Information). A shift in the location of the diffraction peaks and a corresponding change in the unit cell volume, which would be expected if the Zn atoms were incorporated into the CeO_2 lattice, could not be confirmed due to resolution limitation of the XRD patterns (Figure 4). The crystallite sizes determined in the refinements (Table 2, Supporting Information) were consistent with the particle sizes estimated from the TEM analysis and those reported previously.[20] The sizes calculated using the Scherrer equation, based on the peak full-widths of reflections (111) and (101) for CeO_2 and ZnO, respectively, also correlated with the values given here. A correction must be made in the values estimated from the refinements reported in the previous work, recalculated as approximately 4 nm for the CeO_2 crystallites and an average of 30 nm in the case of ZnO crystallites.[20]

dx.doi.org/10.1021/ie3025642 | Ind. Eng. Chem. Res. 2013, 52, 5522−5528

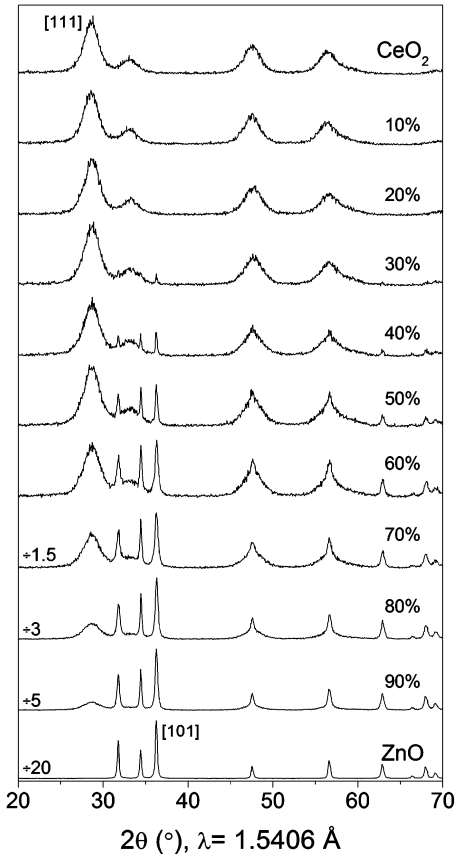

Figure 4. X-ray diffraction patterns of the Zn−Ce oxide system. Nominal Zn content in the mixed oxides is given in mol%. The relative intensity of 70−90 mol% Zn oxides and ZnO patterns is adjusted as indicated. Reflections (111) and (101) have been used in the estimation of crystallite sizes (Scherrer equation) for CeO_2 and ZnO, respectively.

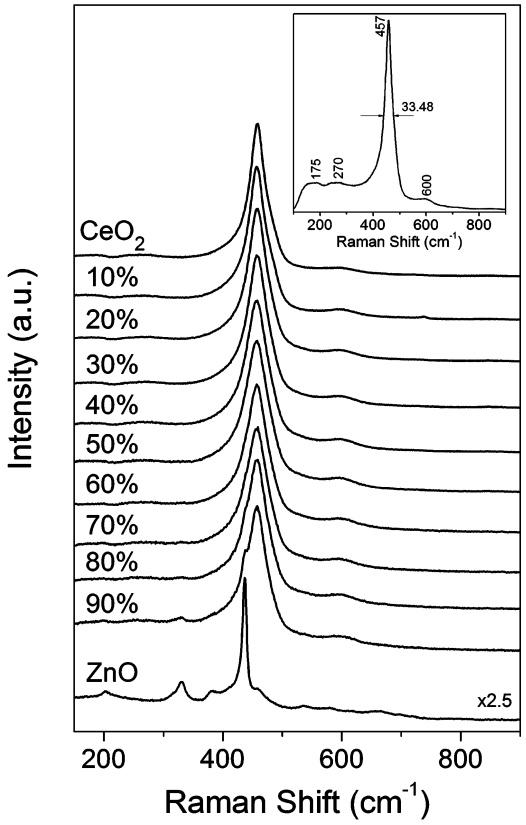

Figure 5. Normalized Raman spectra of the Zn−Ce oxide system, containing an increasing amount of Zn from top to bottom. Nominal Zn content (mol%) and intensity ratio for the ZnO spectrum are indicated. Inset: Raman spectra of pure CeO_2 highlighting the main band full width and band positions.

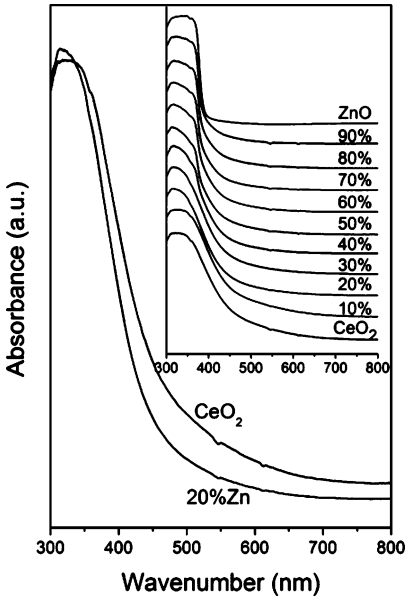

Figure 6. Absorption spectra of CeO_2 and $Zn_{0.2}Ce_{0.8}O_{2-\delta}$. Inset shows normalized absorption spectra of the Zn−Ce oxide system upon nominal Zn content (mol%).

The Raman spectra of all samples are shown in Figure 5. The spectrum of bulk CeO_2 is dominated by a characteristic Ce−O vibration (F_{2g}) at 465 cm^{-1}. Defects related to oxygen vacancies, strain, and phonon confinement induce red shifts and broadening of this band that can be directly related to crystallite size.[35,36] The Raman spectrum of our nanostructured CeO_2 sample showed this band at 457 cm^{-1} and its width was about 33.5 cm^{-1} (Figure 5, inset). The broad Raman bands below 400 cm^{-1} and the spectral features in the 500−600 cm^{-1} region (Figure 5) have been related to oxygen vacancies and dopant defects.[36] The Raman spectrum of ZnO is less intense than the spectrum of CeO_2, and thus, its presence was only noticeable in samples containing above 70 mol% Zn. The spectrum of pure ZnO reaffirmed its wurtzite structure.[37] The crystallite size of CeO_2 can be estimated from Raman data using the linear least-squares fit reported by Weber et al. [Γ (cm^{-1}) = 5 + 518/D (Å), where Γ is the half width of the band].[35] This estimation suggested a particle size of about 4−5 nm, which is consistent with all other size estimates.

The UV−vis absorption spectrum of CeO_2 arises from charge transfer transitions between O 2p and Ce 4f states in O^{2-} and Ce^{4+}, with strong absorption bands at about 270 and 340 nm. However, this spectrum is affected by particle properties and for the reported samples are presented in Figure 6.[38]

The absorption band at 340 nm is very broad for CeO_2 nanoparticles and appears blue-shifted compared to that for bulk CeO_2.[38] Accordingly, the spectrum of the authors' pilot plant CeO_2 sample had a band maximum centered at 330 nm (Figure 6). The optical fibers used in our UV−vis spectrometer setup absorb UV light below 300 nm, and hence, the

dx.doi.org/10.1021/ie3025642 | Ind. Eng. Chem. Res. 2013, 52, 5522−5528

observation of the band at 270 nm was not possible. Introduction of a nominal value of 20 mol% Zn in ceria substantially reduced absorption in the visible region, but a smooth shift between CeO_2-like and ZnO-like spectral profiles was observed thereafter (Figure 6). Direct bandgaps of pure CeO_2, pure ZnO, and mixed the Zn−Ce oxides were estimated using the Kubelka−Munk function (Figure 7), F(R) =

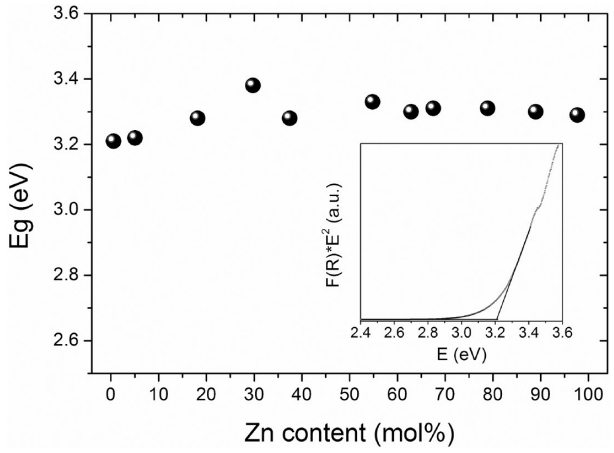

Figure 7. Bandgap shift upon increasing Zn content (mol%) in the Zn−Ce oxide system. The bandgap was estimated using the Kubelka−Munk (KM) function. Inset: Tauc plot for CeO_2 (direct bandgap).

$(1 - R)^2/2R$ (where R is reflectance data). A representative plot showing $F(R) \times E^2$ vs E (where E (eV) is photon energy) is included in Figure 7 (inset).[39] The bandgap of CeO_2 (3.21 eV) was comparable to that reported for nonoriented polycrystalline CeO_2 (3.19 eV) and within the range reported in the literature.[38,40,41] The energy shift observed upon increasing Zn content in the mixed oxide samples showed good correlation with the shift reported in our previous work (Figure 7).[20] In this context, we have used the bandgap as a measure of the averaged absorption properties of the composite (especially in the biphasic region of the sample series). Strictly speaking, we report the average bandgap of the composite that would be composed of the unique bandgaps of both the semiconductors present in the sample, and in this context, we are simply using this as a measure of similarity with a previous sample series.[20]

A sudden initial blue shift can be explained in terms of a smaller particle size within this range, as discussed above.[42] Beyond 50 mol% Zn content, the energy trend reached a plateau around the bandgap of pure ZnO (3.3 eV). Surprisingly, a recent report suggested a significant red shift upon increasing Zn content, with the bandgap of CeO_2 being the largest one (3.35 eV) in their series.[34]

4. CONCLUSIONS AND CLOSING REMARKS

A recently built pilot plant continuous hydrothermal flow synthesis reactor has been presented, representing 17.5 times scale-up (on flow) over an existing laboratory scale process. In this study, the concentrations of the Zn- and Ce-containing precursors were matched to those used in a previous laboratory scale synthesis so that a comparison of the physical properties of the products could be made. Important nanoparticle properties related to the BET surface area, phase behavior, and crystallite size were shown to be virtually indistinguishable from those produced by the laboratory scale apparatus. In particular, the solubility of Zn in the nanoparticle fluorite lattice was observed with a limit of 20−30 mol% (Zn in CeO_2) for the as-prepared nanomaterial and as little as 10−20 mol% Ce into ZnO. Doping Zn into CeO_2 dramatically altered the shape and position of the UV−visible absorption edge, an observation consistent with the previous publication. This similarity was despite the substantive volumetric scale-up of the pilot process and other slight differences in apparatus. This suggests that the processes underlying the nucleation and growth of nanoparticles occur at similar rates, yielding materials showing indiscernible physical characteristics, highlighting that the CHFS process is highly scalable and remains a nucleation dominated process when the output of the process is increased on a volumetric basis alone.[23] A further order-of-magnitude scale up of the process is possible by increasing the concentration of metal salts in the feed precursors, explored in a separate study.[23]

■ ASSOCIATED CONTENT

Supporting Information

Supplementary figures and tables. This information is available free of charge via the Internet at http://pubs.acs.org.

■ AUTHOR INFORMATION

Corresponding Author

*Fax: +44 (0)20 7679 7463. Tel: +44 (0)20 7679 4345. E-mail: j.a.darr@ucl.ac.uk.

Author Contributions

The manuscript was written through contributions of all authors. All authors have given approval to the final version of the manuscript.

Notes

The authors declare no competing financial interest.

■ ACKNOWLEDGMENTS

EPSRC are thanked for funding a project entitled *Continuous Hydrothermal Synthesis of Nanomaterials: From Laboratory to Pilot Plant*; EPSRC reference: EP/E040551/1. The EPSRC are also thanked for funding the access to the TEM instruments in Oxford Materials under the Materials Equipment Access Scheme, Grant EP/F01919X/1, and Dr. John Hutchinson is thanked for taking the HRTEM images. Dr. S. Alexander and Dr. Josephine B. M. Goodall are thanked for technical assistance.

■ REFERENCES

(1) Si, P. Z.; Jiang, W.; Wang, H. X.; Li, Z. F.; Liu, J. J.; Lee, J. G.; Choi, C. J. Large scale synthesis of nitrogen doped TiO_2 nanoparticles by reactive plasma. *Mater. Lett.* **2012**, *68*, 161.

(2) Rao, C. N. R.; Ramakrishna Matte, H. S. S.; Voggu, R.; Govindaraj, A. Recent progress in the synthesis of inorganic nanoparticles. *Dalton Trans.* **2012**, *41*, 5089.

(3) Darr, J. A.; Poliakoff, M. New directions in inorganic and metal-organic coordination chemistry in supercritical fluids. *Chem. Rev.* **1999**, *99*, 495.

(4) Lee, Y. S.; Tay, W. H.; Yap, S. L.; Wong, C. S.; Ahmad, Z. Copper nanoparticle synthesis by the wire explosion technique. *AIP Conf. Proc.* **2009**, *1150*, 452 , Frontiers in Physics, 3rd International Meeting.

(5) Thiébaut, B. Flame spray pyrolysis: A unique facility for the production of nanopowders. *Platinum Metals Rev.* **2011**, *55*, 149.

(6) Nanoscience and Nanotechnologies: Opportunities and Uncertainties; The Royal Society and The Royal Academy of Engineering: London, July, 2004.

(7) Tang, S.; Bourne, R.; Smith, R.; Poliakoff, M. The 24 principles of green engineering and green chemistry: Improvements productively. *Green Chem.* **2008**, *10*, 268.
(8) Ma, C. Y.; Wang, X. Z.; Tighe, C. J.; Gruar, R.; Darr, J. A. Modelling and simulation of counter-current and confined jet reactors for continuous hydrothermal flow synthesis of nano-materials. *Am. Inst. Chem. Eng.*, accepted manuscript.
(9) Zhang, Z.; Goodall, J. B. M.; Brown, S.; Karlsson, L.; Clark, R. J. H.; Hutchinson, J. L.; Rehman, I. U.; Darr, J. A. Continuous hydrothermal synthesis of extensive 2D sodium titanate ($Na_2Ti_3O_7$) nano-sheets. *Dalton Trans.* **2010**, *39*, 711.
(10) Zhang, Z.; Goodall, J. B. M.; Morgan, D. J.; Brown, S.; Clark, R. J. H.; Knowles, J. C.; Mordan, N. J.; Evans, J. R. G.; Carley, A. F.; Bowker, M.; Darr, J. A. Photocatalytic activities of N-doped nano-titanias and titanium nitride. *J. Eur. Ceram. Soc.* **2009**, *29*, 2343.
(11) Thompson, K.; Goodall, J. B. M.; Kellici, S.; Mattinson, J. A.; Egerton, T. A.; Rehman, I. U.; Darr, J. A. Screening tests for the evaluation of nanoparticle titania photocatalysts. *J. Chem. Technol. Biotechnol.* **2009**, *84*, 1717.
(12) Chaudhry, A. A.; Goodall, J. B. M.; Vickers, M.; Cockcroft, J. K.; Rehman, I. U.; Knowles, J. C.; Darr, J. A. Synthesis and characterisation of magnesium substituted calcium phosphate bioceramic nanoparticles made via continuous hydrothermal flow synthesis. *J. Mater. Chem.* **2008**, *18*, 5900.
(13) Weng, X. L.; Boldrin, P.; Abrahams, I.; Skinner, S. J.; Darr, J. A. Direct synthesis of mixed ion and electronic conductors $La_4Ni_3O_{10}$ and $La_3Ni_2O_7$ from nanosized coprecipitates. *Chem. Mater.* **2007**, *19*, 4382.
(14) Weng, X. L.; Brett, D.; Yufit, V.; Shearing, P.; Brandon, N.; Reece, M.; Yan, H.; Darr, J. A. Highly conductive low nickel content nanocomposite dense cermets from nano-powders made via a continuous hydrothermal synthesis route. *Solid State Ionics.* **2010**, *181*, 827.
(15) Weng, X. L.; Zhang, J. Y.; Wu, Z. B.; Liu, Y.; Wang, H. Q.; Darr, J. A. Continous hydrothermal syntheses of highly active composite nanocatalysts. *Green Chem.* **2011**, *13*, 850.
(16) Elouali, S.; Bloor, L. G.; Binions, R.; Parkin, I. P.; Carmalt, C. J.; Darr, J. A. Gas sensing with nano-indium oxides (In_2O_3) prepared via continuous hydrothermal flow synthesis. *Langmuir* **2012**, *28*, 1879.
(17) Lin, T.; Kellici, S.; Gong, K.; Thompson, K.; Evans, J. R. G.; Wang, X.; Darr, J. A. Rapid automated materials synthesis instrument: Exploring the composition and heat-treatment of nanoprecursors toward low temperature red phosphors. *J. Comb. Chem.* **2010**, *12*, 383.
(18) Weng, X. L.; Cockcroft, J. K.; Hyett, G.; Vickers, M.; Boldrin, P.; Tang, C. C.; Thompson, S. P.; Parker, J. E.; Knowles, J. C.; Rehman, I. U.; Parkin, I. P.; Evans, J. R. G.; Darr, J. A. High-throughput continuous hydrothermal synthesis of an entire nanoceramic phase diagram. *J. Comb. Chem.* **2009**, *11*, 829.
(19) Parker, J. E.; Thompson, S. P.; Cobb, T. M.; Yuan, F. J.; Potter, J.; Lennie, A. R.; Alexander, S.; Tighe, C. J.; Darr, J. A.; Cockcroft, J. C.; Tang, C. C. High-throughput powder diffraction on beamline I11 at diamond. *J. Appl. Crystallogr.* **2011**, *44*, 102.
(20) Kellici, S.; Gong, K.; Lin, T.; Brown, S.; Clark, R. J. H.; Vickers, M.; Cockcroft, J. K.; Middelkoop, V.; Barnes, P.; Perkins, J. M.; Tighe, C. J.; Darr, J. A. High-throughput continuous hydrothermal flow synthesis of Zn-Ce oxides: Unprecedented solubility of Zn in the nanoparticle fluorite lattice. *Philos. Trans. R. Soc., A.* **2010**, *368*, 4331.
(21) Adschiri, T.; Lee, Y.-W.; Goto, M.; Takami, S. Green materials synthesis with supercritical water. *Green Chem.* **2011**, *13*, 1380.
(22) Ma, C. Y.; Tighe, C. J.; Gruar, R. I.; Mahmud, T.; Darr, J. A.; Wang, X. Z. Numerical modelling of hydrothermal fluid flow and heat transfer in a tubular heat exchanger under near critical conditions. *J. Supercrit. Fluids* **2011**, *57*, 236.
(23) Gruar, R.; Tighe, C. J.; Darr, J. A. Scaling-up a confined jet reactor for the continuous hydrothermal manufacture of nanomaterials. *Ind. Eng. Chem. Res.* **2012**, 10.1021/ie302567d.
(24) Morinaga, Y.; Sakuragi, K.; Fujimura, N.; Ito, T. Effect of Ce doping on the growth of ZnO thin films. *J. Cryst. Growth* **1997**, *174*, 691.
(25) Li, R. X.; Yabe, S.; Yamashita, M.; Momose, S.; Yoshida, S.; Yin, S.; Sato, T. Synthesis and UV-shielding properties of ZnO- and CaO-doped CeO_2 via soft solution chemical process. *Solid State Ionics* **2002**, *151*, 235.
(26) Yang, J.; Gao, M.; Yang, L.; Zhang, Y.; Lang, J.; Wang, D.; Wang, Y.; Liu, H.; Fan, H. Low-temperature growth and optical properties of Ce-doped ZnO nanorods. *App. Surf. Sci.* **2008**, *255*, 2646.
(27) Wang, L. S.; Xiao, M. W.; Huang, X. J.; Wu, Y. D. Synthesis, characterization and photocatalytic activities of titanate nanotubes surface-decorated by zinc oxide nanoparticles. *J. Hazard. Mater.* **2009**, *161*, 49.
(28) Chai, X.; Wang, D. UV-shielding and catalytic characteristics of nanoscale zinc-cerium oxides. *J. Wuhan Univ. Technol., Mater. Sci. Ed.* **2007**, *22*, 622.
(29) El Jouad, M.; Lamrani, M. A.; Sofiani, Z.; Addou, M.; El Habbani, T.; Fellahi, N.; Bahedi, K.; Dghoughi, L.; Monteil, A.; Sahraoui, B.; Dabos, S.; Gaumer, N. Roughness effect on photo-luminescence of cerium doped zinc oxide thin films. *Opt. Mater.* **2009**, *31*, 1357.
(30) Kockrick, E.; Schrage, C.; Grigas, A.; Geiger, D.; Kaskel, S. Synthesis and catalytic properties of microemulsion-derived cerium oxide nanoparticles. *J. Solid State Chem.* **2008**, *181*, 1614.
(31) Ge, C.; Xie, C.; Cai, S. Preparation and gas-sensing properties of Ce-doped ZnO thin-film sensors by dip-coating. *Mater. Sci. Eng., B* **2007**, *137*, 53.
(32) Evans, J. R. G. Seventy ways to make ceramics. *J. Eur. Ceram. Soc.* **2008**, *28*, 1421.
(33) B.G. Mishra, B. G.; Rao, G. R. Promoting effect of ceria on the physicochemical and catalytic properties of CeO_2. *J. Mol. Catal. A: Chem.* **2006**, *243*, 204.
(34) Ma, T.-Y.; Yuan, Z.-Y.; Cao, J. L. Hydrangea-like meso-/macroporous ZnO-CeO_2 binary oxide materials: synthesis, Photo-catalysis and CO oxidation. *Eur. J. Inorg. Chem.* **2010**, *5*, 716.
(35) Spanier, J. E.; Robinson, R. D.; Zhang, F.; Chan, S.-W.; Herman, I. P. Size-dependent properties of CeO_{2-y} nanoparticles as studied by Raman scattering. *Phys. Rev. B* **2001**, *64*, 245407.
(36) Weber, W. H.; Hass, K. C.; McBride, J. R. Raman study of CeO_2: Second-order scattering, lattice dynamics and particle-size Effects. *Phys. Rev. B* **1993**, *48*, 178.
(37) Damen, T. C.; Porto, S. P. S.; Tell, B. Raman effect in zinc oxide. *Phys. Rev.* **1966**, *142*, 570.
(38) Ho, C.; Yu, J. C.; Kwong, T.; Mak, A. C.; Lai, S. Morphology-controllable synthesis of mesoporous CeO_2 nano- and microstructures. *Chem. Mater.* **2005**, *17*, 4514.
(39) Tauc, J. Optical properties and electronic structure of amorphous Ge and Si. *Mater. Res. Bull.* **1968**, *3*, 37.
(40) Corma, A.; Atienzar, P.; García, H.; Chane-Ching, J.-Y. Hierarchically mesotructure doped CeO_2 with potential for solar-cell use. *Nat. Mater.* **2004**, *3*, 394.
(41) S. Phoka, S.; Laokul, P.; Swatsitang, E.; Promarak, V.; Seraphin, S.; Maensiri, S. Synthesis, structural, optical properties of CeO_2 nanoparticles synthesized by a simple polyvinyl pyrrolidone (PVP) solution route. *Mater. Chem. Phys.* **2009**, *115*, 423.
(42) Tsunekawa, S.; Wang, J.-T.; Kawazoe, Y.; Kasuya, A. Blueshifts in the ultraviolet absorption of cerium oxide nanocrystallines. *J. Appl. Phys.* **2003**, *94*, 3654.